

Ultra-Wideband Imaging Systems for Breast Cancer Detection

Hossein Kassiri Bidhendi, Hamed Mazhab Jafari and Roman Genov

Abstract In this chapter we will begin with an introduction to ultra-wideband (UWB) communication systems and their application in medical imaging. The rest of the chapter will present design of UWB receiver and transmitter blocks (low-noise amplifier (LNA), Multiplier and pulse generator) that are designed, fabricated and tested by authors. The reader will have a good understanding of a UWB transceiver system design and its advantages for breast cancer detection after reading this chapter.

Keywords Breast cancer detection · Breast imaging · Ultra-wideband imaging · UWB transceiver · UWB pulses · UWB transmitter · UWB receiver

Motivation

Worldwide breast cancer is one of the leading causes of death among women. Only in the USA, tens of thousands of deaths are reported yearly because of this type of cancer. 26 percent of all types of cancers among women are breast cancer [1]. It is now well-known that a high percentage of patients with this type of cancer can be cured if diagnosed in the early stages. There are many ongoing research projects to develop and improve imaging systems to help early detection of this type of cancer. This includes works which are concentrated on improvement of image processing or imaging system optimization using new technologies.

Ultra-wideband (UWB) communications is one of the newest technologies employed in imaging systems that are utilized for human's body imaging. The motivation is mainly based on using ultra-narrow pulses in the time domain to detect and contrast between normal and malignant tissues. This has initiated many research projects based on using this technology for imaging of a particular organ of body including heart, lung, breast, and organs involved in breath and speech mechanisms [2].

H. K. Bidhendi (✉) · R. Genov · H. M. Jafari
Department of Electrical and Computer Engineering,
University of Toronto, Toronto, ON M5S 3G4, Canada
e-mail: hkassiri@eecg.utoronto.ca

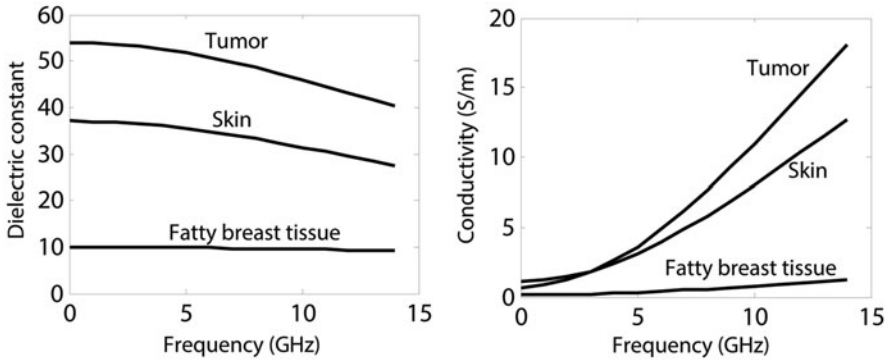


Fig. 1 Frequency dependence of the dielectric constant and conductivity for fatty breast tissue, skin, and tumor. [7]

The main motivation for using ultra-narrow pulses for breast imaging arises from the high contrast between the electrical properties of malignant and normal breast tissues. For instance, this contrast is 5:1 for relative dielectric constant and 10:1 for conductivity at microwave frequencies [3, 4] (see Fig. 1). In addition to contrast, UWB microwave imaging systems are also able to provide both adequate penetration depth and necessary imaging resolution [5, 6].

Medical Imaging for Breast Cancer

Among various types of medical imaging applications of UWB systems, breast cancer detection is one of the most popular fields that has attracted much research interest. In recent years, an increasing number of deaths due to breast cancer are reported. Only in the USA, there is an average of 40,000 deaths a year because of this type of cancer [8]. Since curing this type of cancer or long-term survival of patients are highly dependent on early detection and timely medical intervention, a very precise and dependable imaging system is required in the treatment procedure.

Conventional mammography has been performed using x-ray imaging of a compressed breast for nonpalpable early stage breast cancer [9]. Throughout the time, some technical advancements, such as digital mammography plus radiological expertise, have provided significant improvement of image quality and diagnosis using x-ray. However, due to sensitivity issues of x-ray imaging, there are still many problems with relatively high false-negative rate of detection, and low positive predictive rates resulting in many additional unnecessary biopsies [10]. In addition, in x-ray imaging, patients have to deal with uncomfortable or painful breast compression and exposure to low level ionization.

Usually, magnetic resonance imaging (MRI) and ultrasound are used for verification of mammography detected lesions by x-ray. In these systems, the modalities are not yet sensitive/specific enough or are too operator dependent or too costly to be useful for screening purposes.

All of above limitations have led to efforts to find an alternative to x-ray mammography. One of the most promising alternatives is using microwave imaging with UWB systems. As mentioned before, for the radio frequency (RF) and the microwave range of frequencies, differences in electrical characteristics of malignant and normal tissues are greater than 2:1. Also, dielectric constant, ϵ_r , and conductivity, σ , change with increasing water content in neoplastic tissues due to increased protein hydration [11]. This fact will result in exploiting strong indicators of malignancy associated with physical or physiological factors of clinical interest such as water content, vascularization, blood flow rate, and temperature.

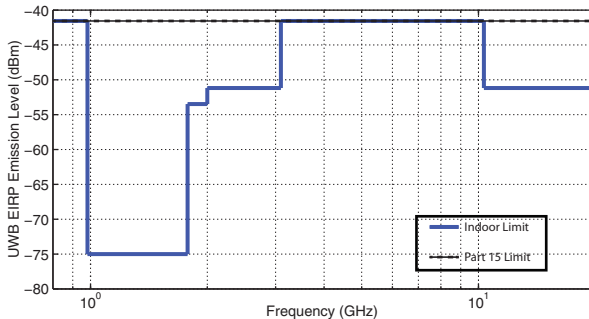
This advantage over x-ray can compensate for spatial resolution of UWB systems which is not as good as x-ray imaging because of the wavelength difference. In fact, high contrast exists for both high and low frequencies. At lower frequencies, the contrast is due to breakdown of narcotic cell membranes which are being used for electrical impedance topography [12, 13]. On the other hand, at higher frequencies, there will be high contrast due to increase in DNA, protein, and hemoglobin absorption in malignant tissues [14]. Considering the above advantages of working in different frequencies and after studying parameters which are important in an imaging procedure, it has been concluded that the frequency range between 1 and 10 GHz is the optimum band for this application. This band is a range that includes both advantages of having high spatial resolution which is better at higher frequencies and also good penetration depth which is better for lower frequencies.

Today, it is well known that microwave imaging is a promising substitute for conventional mammography. It is also known what frequency range should be used for imaging. From this perspective, there have been two main techniques for active microwave imaging: radar and tomography. Both techniques are based on the dielectric contrast in this range of frequency. In both techniques, low-power microwave signals are transmitted from an array of antennas into the breast. The tomographic image reconstruction technique is the most commonly attempted technique in this frequency range that can be performed using narrowband signals. In this technique, an image reconstruction problem should be solved, which needs regularization to converge and have a meaningful solution. However, many of these concerns are minimized in smaller form-factor cases like that in breast cancer detection. On the other hand, there is UWB radar in which there is no effort to reconstruct the complete profile of dielectric properties of the breast. In fact, in this technique, the goal is to find the presence and location of significant backscattered energy due to difference in dielectric properties of normal and malignant tissues.

In general, the microwave frequency domain for breast imaging is associated with the following features that are expected from a UWB system as an imaging system working in this range of frequency:

1. Significant contrast between dielectric properties of normal and malignant tissues in this frequency range. In normal tissues of the breast, microwave attenuation is low enough that we can image the entire breast.
2. Avoiding breast compression, as well as using low-power signals which result in little health risk.

Fig. 2 Ultra-wideband emission limit for indoor systems. [17]



3. Conventional microwave tomography has computational challenges. Using space-time UWB imaging, these problems can be solved and a very good three-dimensional picture of the breast can be obtained.
4. Using space-time UWB imaging systems, a precision of less than 0.5 cm is expected which is good enough for early detection and localization of breast cancer.
5. Finally, UWB microwave imaging is able to detect if the lesion is malignant or benign. For benign lesions, the dielectric properties are not different from normal tissues as much as they are for malignant lesions. As a result, the scattered waves are not as strong as they are for malignant tissues.

Ultra-Wideband Technology for Breast Cancer Detection

UWB is a communication technology that can achieve high data rates of up to 1 Gbps, uses very low power pulses and is suitable for short-distance applications [15, 16].

Due to the use of short pulses which results in high multi-path resolution, UWB systems do not have problems with fading, which is a serious problem in narrowband systems. Furthermore, because of the wideband nature of these systems, power is distributed over a wide range of frequency, which results in a very low power level at each frequency. Consequently, less interference with other RF systems is expected. In 2002, the Federal Communication Commission (FCC) authorized commercial use of the band from 3.1 to 10.6 GHz for research and technology development of new electronic systems. Although different narrowband radio systems operate in this range of frequency, as long as UWB systems satisfy FCC's spectral mask, they can coexist with narrowband systems. For indoor applications, this mask is shown in Fig. 2 and Fig. 3. As shown, maximum equivalent isotropic radiated power (EIRP) spectral density which is allowed by FCC is -41.3 dBm/MHz. This mask suggests interesting short-distance applications for UWB range. On the other hand, high spatial resolution of this technology makes it a promising candidate for medical imaging.

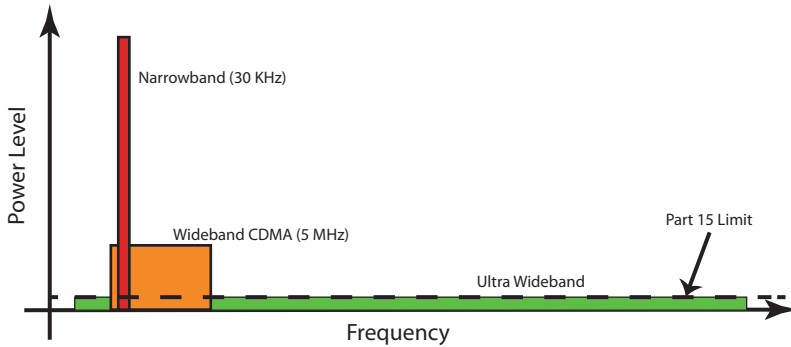


Fig. 3 Power level of ultra-wideband system in comparison with narrowband and wideband systems. [17]

Fig. 4 The hemispherical configuration used for breast cancer detection. [7]

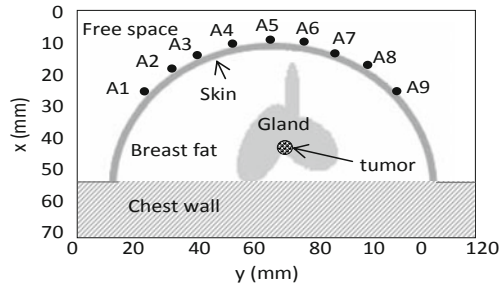
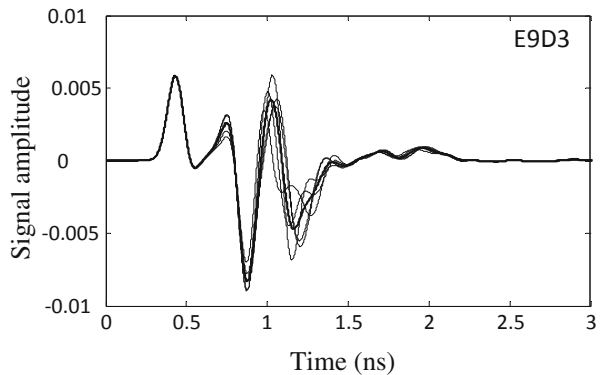


Fig. 5 Detected signal for different positions of tumor. Thick solid line is the average of calibration waveform. [7]



The basic idea of breast cancer detection is to send an ultra-narrow low-power pulses to the patient’s body and make a decision based on the received signal by comparing it with a reference signal, average of backscattered signals, or a signal backscattered from normal tissues. Figure 4 shows an example in which nine antennas are positioned on a human’s breast in a hemi-spherical configuration. First, as shown in Fig. 5, different pulses will be emitted from each of the antennas and detected by another antenna and location of simulated tumor is being randomly changed. Then,

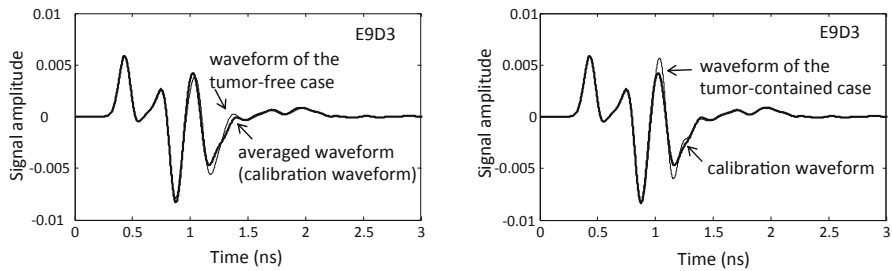


Fig. 6 Received signals compared with average waveform for two cases of normal and malignant tissues. [7]

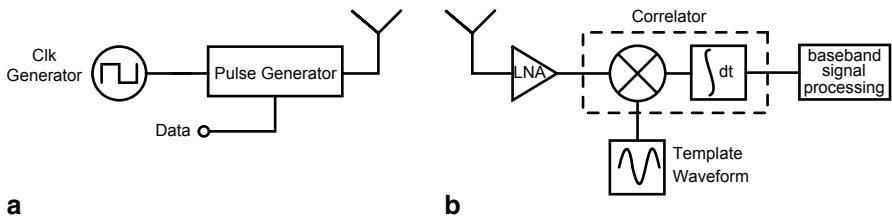


Fig. 7 Typical transceiver of an ultra-wideband system

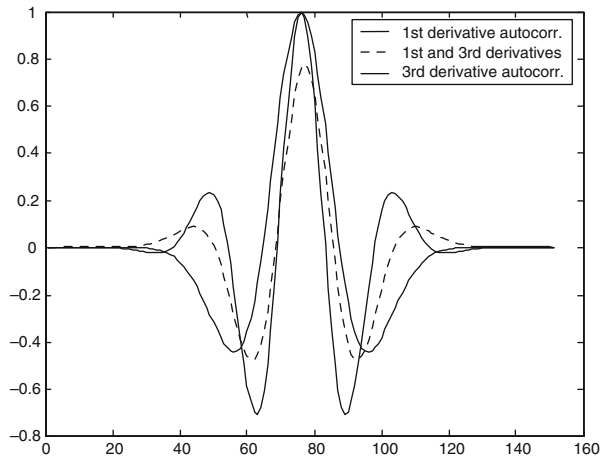
an average waveform of the received signals is calculated. The next step is comparing the received signals with this waveform, which indicates the probability of a tumor existing in a specific location. Figure 6 shows two cases of normal and malignant tissues. As shown, for the malignant tissue, differences between received signal and the average (calibration) waveform is much higher than for the normal tissue.

Figure 7 shows a symbolic block diagram of UWB medical imaging system for breast cancer detection. As shown, a UWB medical imaging system has major differences when compared with narrowband systems. First, since there is no carrier in this type of communication, there is no need for complicated modulation and demodulation blocks. These are among the most complicated blocks used for conventional continuous wave transmission systems. Not having these complex components makes the transmitter architecture of UWB systems inexpensive, simpler to design, and simpler to implement, when compared to conventional radio systems.

From this point of view, a UWB system’s block diagram is much simpler than its narrowband counterparts. As shown in Fig. 7, in UWB systems, time-domain modulation is used for transmitting and receiving data. This makes the correlation and sample waveform generator blocks of this system very important.

According to the work by Proakis et al. [18], the optimal receiver for a signal transmitted in an additive white Gaussian noise (AWGN) channel is a correlation or a matched filter receiver which makes SNR (signal to noise ratio) maximum. Figure 7b shows a receiver architecture that is made of three major blocks: a low-noise amplifier (LNA), a correlation circuitry and a block for providing template waveform for correlation circuit. In addition, there is also the baseband signal processing unit in which the decision making is performed.

Fig. 8 Correlation results of transmitted and received signals. [20]



The first step in signal detection is to amplify the received signal. If the received signal from the antenna is fairly noisy and weak, then the first stage of the receiver, which is responsible for amplification, must be very low-noise. Also, it should be perfectly matched to the output impedance of the antenna, which is normally 50Ω .

The next stage is the correlation block in which the amplified signal is compared to the template waveform. Generating a good template waveform is one of the most important issues in UWB receiver design for the correlator block. In fact, this waveform should be as similar to the received signal as possible, to maximize signal-to-noise ratio which is a complicated task. One option is to approximate the received waveform by the transmitted signal. Second way is a coarse approximation such as a rectangular wave, which is very simple to generate but is not very efficient.

Another approach, which is proposed in [19] is to ignore the template waveform and to rely on the finite bandwidth of the transmitting and receiving antennas, which results in a specific pulse shaping. Both transmitting and receiving antennas work as differentiators. As a result, in ideal conditions, the received signal in the receiver must be the second derivative of the transmitted signal. For the UWB pulse, this means the third derivative of a Gaussian pulse. In [20], the autocorrelation of the first and second derivatives of a Gaussian pulse are compared. Also, the crosscorrelation of the first and third derivatives of this pulse are compared to the autocorrelation results. The results in Fig. 8 show that the crosscorrelation results have an almost 80 percent accuracy of the third derivative autocorrelation which means a loss of less than 1 dB, which is quite tolerable for this application.

The template waveform is multiplied by the input signal and gets integrated over the bit duration to maximize the received signal power and minimize the noise component. Consequently, for a pulse train, the integrator's results will be higher than the noise level and the desired signal can be detected and separated from unwanted signals. It should be noted that the architecture introduced above will be different for other types of applications. For example, many UWB systems use time-hopping pulse

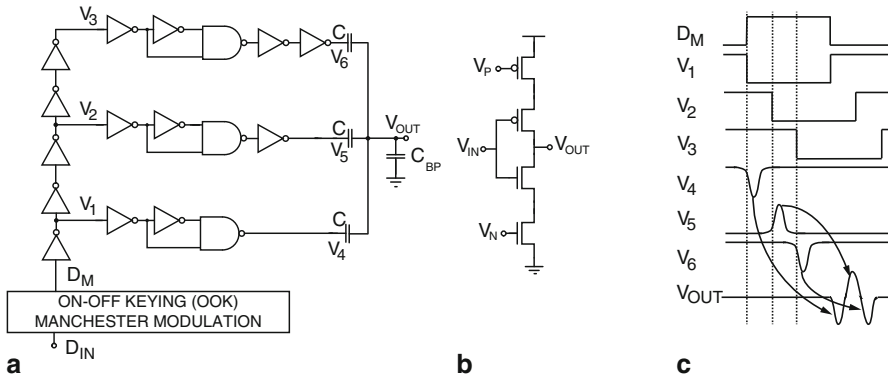


Fig. 9 **a** Ultra-wideband (UWB) transmitter circuit schematic diagram, **b** schematic of one current-starved inverter, and **c** timing diagram of the UWB transmitter

position modulation (TH-PPM) or some other time-domain modulation schemes which should be considered in the transmitter architecture. Also the correlator architecture is not always exactly similar to what was explained here, and it might vary due to the needs of the specific system.

Design Example for Ultra-Wideband Transmitter

The circuit diagram of the all-digital pulsed UWB transmitter is shown in Fig. 9. The input data are modulated using on–off keying (OOK) Manchester modulation. UWB pulses are generated on the rising edge of the modulated data (D_M). A delay line bank is employed together with a capacitively coupled output combiner [21] as shown in Fig. 9a.

The modulated data are passed through a delay line and a delayed version of the data is passed through three pulse generators. The pulse generators shape a first-order Gaussian pulse at the rising edge of the input data. The presented digital UWB transmitter achieves both power efficiency and spectral compliance in a much smaller chip area compared to other designs [22–23]. As illustrated in Fig. 9c, each pulse generator forms pulses that are delayed, and have opposite signs. By capacitively combining the three paths, the opposite signs are canceled, and the zero-DC double differentiated Gaussian pulse propagates to the single-ended antenna. The width of the output pulse depends on the delays in the delay line. The delay cells in all the paths are implemented as current-starved inverters, shown in Fig. 9b, to allow for tuning of the UWB pulse width. The input Manchester-encoded data to the UWB transmitter and its measured output UWB pulses are shown in Fig. 10.

The UWB pulses are measured using custom-built UWB antennas (5 cm spacing between the transmitter and receiver) and a custom-built receiver. A zoomed-in version of one such measured UWB pulse overlaid on a simulated UWB pulse is

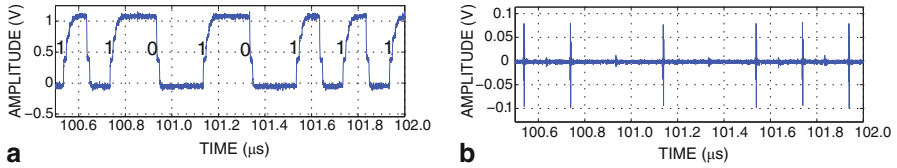


Fig. 10 Experimentally measured **a** Manchester-encoded input data to the ultra-wideband transmitter and **b** the output pulses

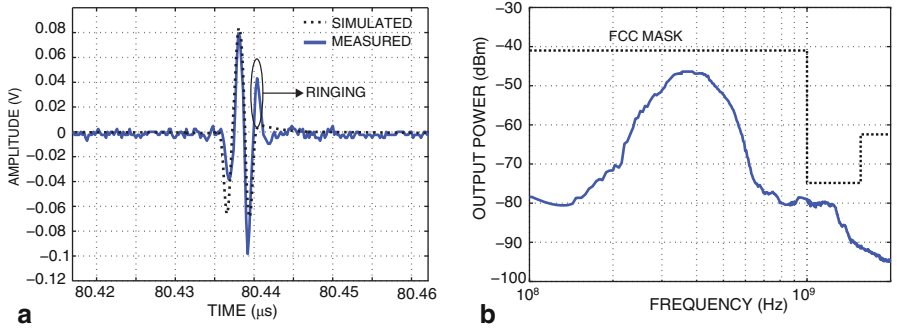


Fig. 11 **a** Wirelessly measured ultra-wideband (UWB) pulse at the distance of 5 cm using a custom-built UWB receiver, and **b** experimentally measured UWB transmitter output spectrum (direct output of the transmitter driving a 50 Ω load). The output spectrum is compliant with the 0–1 GHz Federal Communication Commission (FCC) UWB band output power criteria

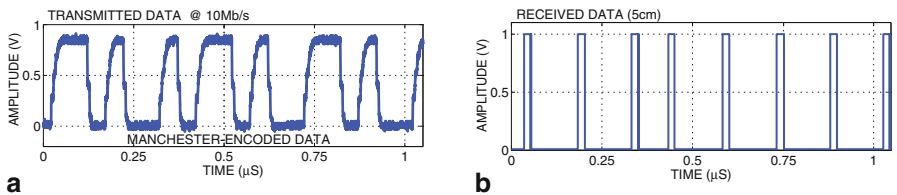
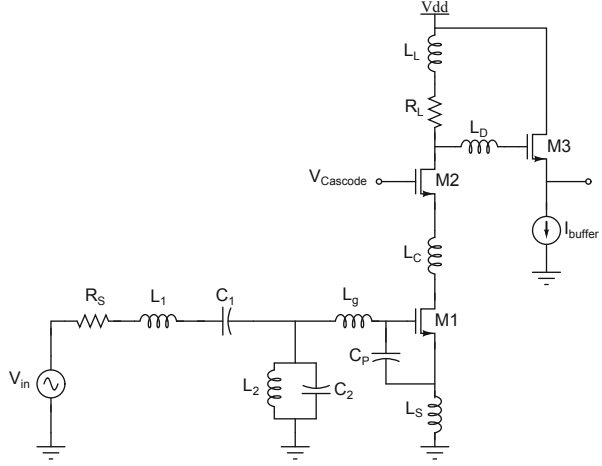


Fig. 12 **a** Manchester-encoded input data to the UWB transmitter and **b** the corresponding data received wirelessly at a 5 cm distance

shown in Fig. 11a. As it can be seen, the measured pulse resembles the expected UWB pulse but includes minor ringing due to the package bondwire inductance. The measured output power spectrum of the UWB transmitter is plotted in Fig. 11b. The power spectrum complies with the FCC-defined 0–1 GHz UWB spectrum (mask) also shown. The same circuit also generates pulses in the 3.1–10.6 GHz range. An example of the input data to the UWB transmitter Manchester-encoded at the rate of 10 Mb/s and the data received at the distance of 5 cm using a custom-built UWB receiver is shown in Fig. 12.

Fig. 13 Low-noise amplifier (LNA) circuit schematic together with the added inductors



Design Example for Ultra-Wideband Receiver

The general block diagram of a UWB receiver was introduced previously in Fig. 7. In this section, an example design and implementation of a UWB LNA and a mixer as two of the most important blocks of the receiver will be presented.

Ultra-Wideband Low-Noise Amplifier

Gain and Bandwidth

In the design presented, a CS (Common Source) configuration with inductive de-generation and a multi-section reactive network for input matching is utilized. The matching network is first proposed in [24]. Also, two auxiliary inductors are added to boost the bandwidth of the amplifier. In the circuit shown in Fig. 13, the drain current i_d can be written as

$$i_d = \frac{V_G g_m}{s(C_p + C_{gs})\omega_t L_s} = \frac{F(s)V_{in}g_m}{s(C_p + C_{gs})\omega_t L_s}, \quad (1)$$

assuming $F(s)$ is the Chebyshev filter transfer function. In the above analysis, C_{gd} is not taken into account. This is mainly because of the very low impedance of the cascode stage seen from drain of M_1 . This will result in very weak Miller effect on gate of M_1 , so C_M is

$$C_M = C_{gd}(1 + g_m(r_o \parallel R_L)). \quad (2)$$

Here, $R_L = 1/g_{m2}$ is small enough to make the Miller capacitance negligible, so the LNA gain without considering L_D and L_C will be

$$\frac{v_{out}}{v_{in}} = \frac{-F(s)g_m}{s(C_p + C_{gs})\omega_t L_s} * \frac{(sL_L + R_L)}{1 + sR_L(C_{db2} + C_{gd3}) + s^2L_L(C_{db2} + C_{gd3})}. \quad (3)$$

Taking L_D and L_C into account, the gain equation of the LNA becomes

$$\frac{v_{out}}{v_{in}} = \frac{-F(s)g_m}{s(C_p + C_{gs})\omega_1 L_s} * \frac{(R_L + sL_L)(1 + s^2 L_D C_{gd3})}{1 + sR_L C_{gd3} + s^2(L_L + L_D)C_{gd3} + C_{gb2}(R_L + sL_L)(s^2 L_D C_{gd3} + 1)}. \quad (4)$$

Comparing two gain equations, it can be concluded that adding the peaking inductors has resulted in removal of one of amplifier's dominant poles which was located at M_2 's drain.

This has been done by breaking parasitic capacitance of this node, ($C_{db2} + C_{gd3}$), into two smaller capacitors. From another point of view, if the step response of this circuit is considered, then isolating the buffer stage from the cascode stage and splitting these two capacitors from each other, results in a much smaller capacitance to be charged and discharged every cycle. This means shorter transient time in the time domain or wider bandwidths in the frequency domain.

Figure 14 shows the pole-zero analysis and the effect of adding L_D . Based on this plot, L_D should be designed in a way such that undesired poles and zeros will be removed. In this work, L_D was designed in such a way that the added poles are located at 7.4 and 9.2 GHz and zeros at 5.9 (twin) and 7.6 GHz. The pole at 7.4 GHz and the zero at 7.6 GHz are close enough to approximately cancel each other's effect and consequently would not have any significant effect on the gain curves. In contrast, the zero at 5.9 GHz, which is a twin zero, not only prevents the gain from decreasing at higher frequencies, but it also results in an increase of the gain amplitude for frequencies beyond 5.9 GHz. This increase will continue until the next twin pole at 9.2 GHz, which stops the gain increment and causes a decrease in the gain until the end of bandwidth. Although the gain amplitude and bandwidth is improved significantly, the gain is still not very flat.

Figure 15 shows the gain curves in different stages of design. Figure 15a is the original design without any additional inductances, Fig. 15b shows the effect of adding L_D and Fig. 15c the effect of both L_D and L_C . The problem with flatness is basically due to the parasitics generated by the cascode stage. The addition of an inductor between the gain and cascode stages will help to improve the gain flatness. In fact, L_C , together with C_{gd1} and C_{gs2} , can form a wideband π -section LC network. As a result, it can resonate with the capacitors to produce broadband operation for the LNA. Figure 14b shows that adding L_C has caused three sets of poles to be relocated and also one set of poles to be generated. Among the three poles that have been displaced, two of them do not have a significant effect. The first is a pole at 8.3 GHz which is moved to 8.1 GHz and the other one is the pole which is moved from 7.5 to 7.9 GHz. In contrast, the third pole displacement is moving the undesirable pole out of the band and it is very effective in improving the gain curve. This pole is moved from 8.94 to 10.9 GHz. The most important effect of L_C is the pole which is generated at 6.13 GHz. This pole is designed to be very close to the twin-zero generated due to the addition of L_D , and it can cancel one of the zeros. As a result,

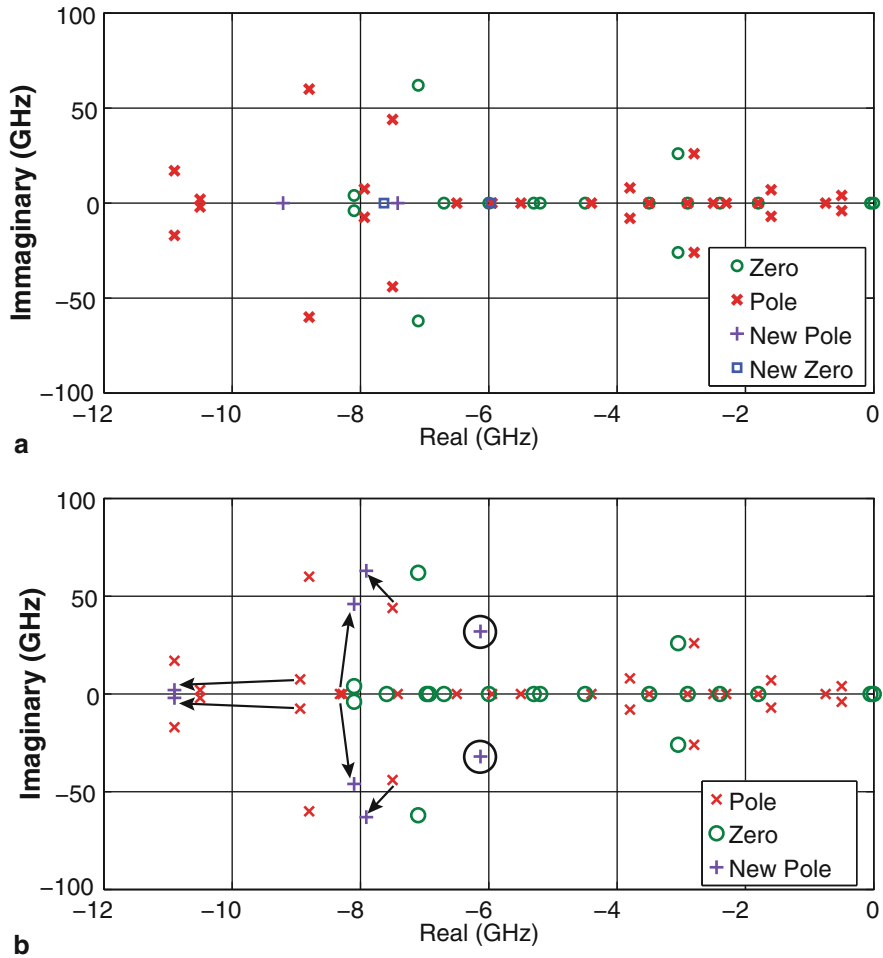


Fig. 14 a Pole-Zero analysis results after addition of L_D and b after addition of both L_D and L_C

there will be no gain increment from 6.13 GHz, until 9.2 GHz, which is the start of the gain decrease.

Noise Figure

There are two important factors that determine the noise of this low-noise amplifier. First are the losses of input matching network, and second is the input transistor M_1 . Generally, the noise of the input matching filter, which is basically due to nonidealities of its reactive components, is negligible in comparison with the noise of the other stages.

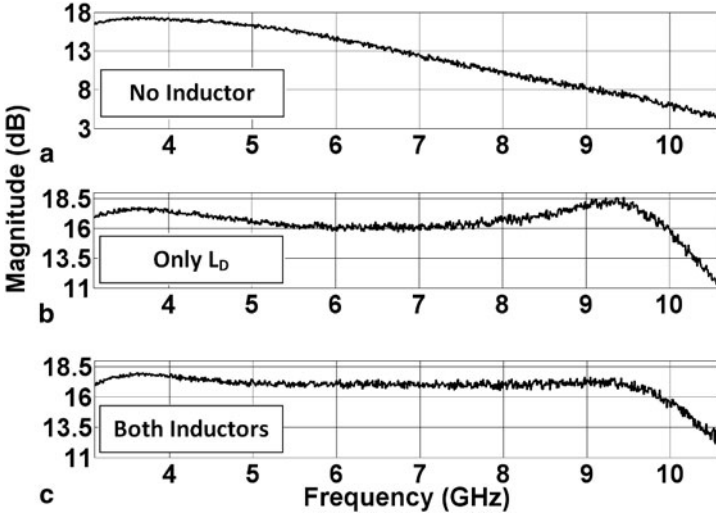


Fig. 15 **a** S_{21} for the original circuit, **b** after addition of L_D , and **c** after addition of both L_D and L_C

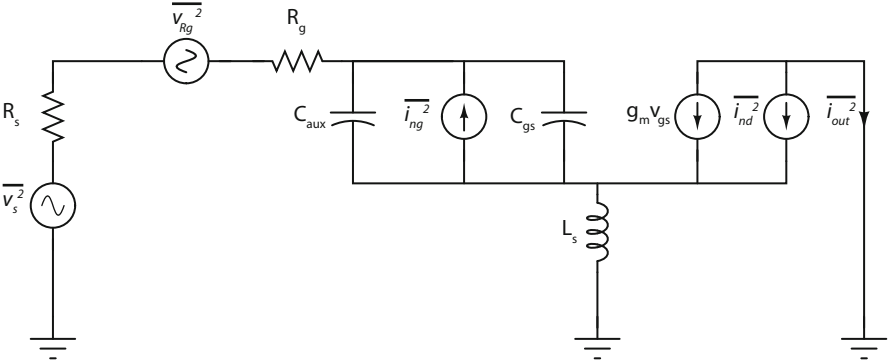


Fig. 16 Noise model for the first stage of designed low-noise amplifier

Furthermore, due to high gain of the first stage, the noise contribution of the cascode and output stages are much smaller than the first stage. As a result, it is assumed that the first stage noise is dominant, and only this noise is considered in calculations. Figure 16 shows a model for the noise of LNA's first stage. Based on this model,

$$\begin{aligned}
 F = 1 + & \frac{\overline{v_{R_g}^2} |G_m(j\omega)|^2 + \overline{l_{ng}^2} |T(j\omega)|^2 + \overline{l_{nd}^2} |D(j\omega)|^2}{\overline{v_g^2} |G_m(j\omega)|^2} \\
 & + \frac{\overline{l_{ng} l_{nd}^*} T(j\omega) D^*(j\omega) + \overline{l_{nd} l_{ng}^*} D(j\omega) T^*(j\omega)}{\overline{v_s^2} |G_m(j\omega)|^2}
 \end{aligned} \quad (5)$$

with,

$$|G_m(j\omega_0)|^2 = \frac{g_m^2}{\omega_0^2 C_t^2 \left(R_s + R_g + \frac{g_m L_s}{C_t} \right)^2}, \quad D(j\omega_0) = \frac{R_s + R_g}{R_s + R_g + \frac{g_m L_s}{C_t}}, \quad (6a)$$

$$T(j\omega_0) = \frac{R_s + R_g + j\omega_0(L_g + L_s)}{R_s + R_g + \frac{g_m L_s}{C_t}} \times \frac{g_m}{j\omega_0 C_t}. \quad (6b)$$

Replacing these terms in (5) and with some simplifications, F will be

$$F = \frac{R}{R_s} \left(1 + R \frac{\gamma \omega_0^2 C_t^2}{\alpha^2 g_{d0}} x \right), \quad (7)$$

where

$$\begin{aligned} x &= \frac{\alpha^2 \delta}{5\gamma} (1 + Q_s^2) \frac{C_{gs}^2}{C_t^2} + 1 - 2|c| \frac{C_{gs}}{C_t} \sqrt{\frac{\alpha^2 \delta}{5\gamma}}, \quad \alpha = \frac{g_m}{g_{d0}}, \\ Q_{s0} &= \frac{1}{\omega_0 C_{gs} R_s}, \quad \omega_\tau = \omega_{\tau 0} \frac{C_{gs}}{C_t} = \frac{g_m}{C_t}, \\ Q_s &= Q_{s0} \frac{C_{gs} R_s}{C_t R} = \frac{1}{\omega_0 C_t R}, \quad R = R_s + R_g, \\ C_t &= C_{gs} + C_{aux}, \quad R = R_s + R_g, \quad \text{and} \quad \omega_{\tau 0} = \frac{g_m}{C_{gs}}. \end{aligned} \quad (8)$$

Based on above equations, the noise figure is optimized with gain and power considerations.

The testchip is designed, fabricated, and tested in a 0.13 μm complementary metal-oxide semiconductor (CMOS) process. Figure 17 shows the measured S-parameters of this circuit. As shown, excellent input and output matching as well as output-to-input isolation are achieved. Peak value of 18.1 dB is measured for S_{21} with excellent gain flatness. Figure 18a shows the measured group delay of the designed LNA. Figure 18b shows the measured IIP3 of this circuit. The intercept point in -1 dBm shows very good linearity. Also, Fig. 18c shows the noise figure of this circuit, with a minimum value of 3.12 dB and an average of 3.81 dB.

Ultra-Wideband Mixer

Despite all the advantages of UWB systems, their design is typically very challenging due to the fact that they should demonstrate good performance for the entire bandwidth. Power consumption, conversion gain, linearity, silicon area, and noise figure are major concerns in the design of UWB mixers.

For Gilbert cells, which are the most common topology of mixers, an increase in the bias current of RF stage will typically result in a better noise performance as well

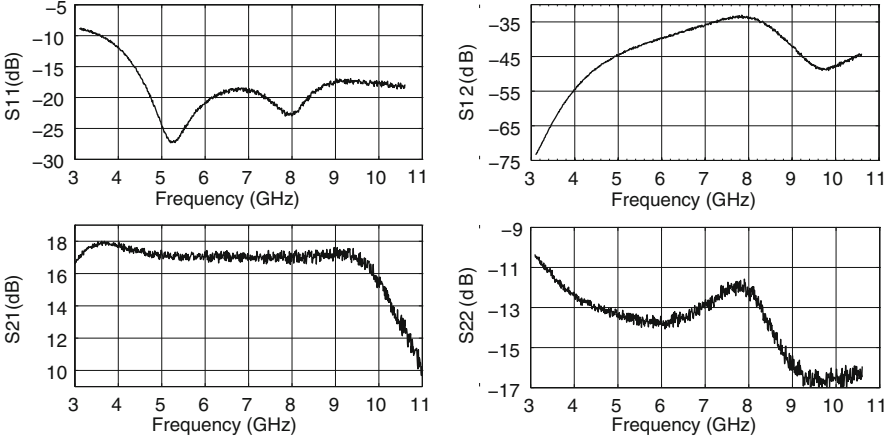


Fig. 17 Measured S-parameters of the designed low-noise amplifier (LNA)

as better linearity and higher transconductance of this stage. Clearly, this will cause a trade-off between power and other performance parameters. One approach that designers took is using current bleeding technique [25, 26] to improve noise, gain, and linearity without dramatic power increase. Using this method is typically limited to narrowband applications; and for UWB, several inductors should be used which results in dramatic area increase. A popular method to overcome this trade-off is to use a folding architecture. There are a number of works [27, 28] that have utilized this topology and achieved good bandwidth without sacrificing area or power. Using a folded architecture, DC current of RF and local oscillator (LO) stages do not have to be equal which results in more degrees of freedom in biasing and consequently a better trade-off. The constraint will be even more relaxed when the biasing of RF and LO stages are isolated.

Figure 19 shows the designed UWB mixer. As shown, a folded architecture with p-type metal-oxide semiconductor (PMOS) LO-stage and inverter RF stage is chosen. In conventional Gilbert cell topology, where RF and LO stages are stacked on top of each other, the bias currents of both stages are tightly correlated which results in a trade-off in performance parameters. For Gilbert cell, the conversion gain can be written

$$CG \propto g_{m,RF} R_L, \quad (9)$$

where, $g_{m,RF}$ represents transconductance of the RF stage and R_L is the load resistance. Also the input referred intercept point (IIP3) can be expressed as

$$IIP3 = 4 \sqrt{\frac{I_{DC,RF}}{3K_{RF}}}, \quad (10)$$

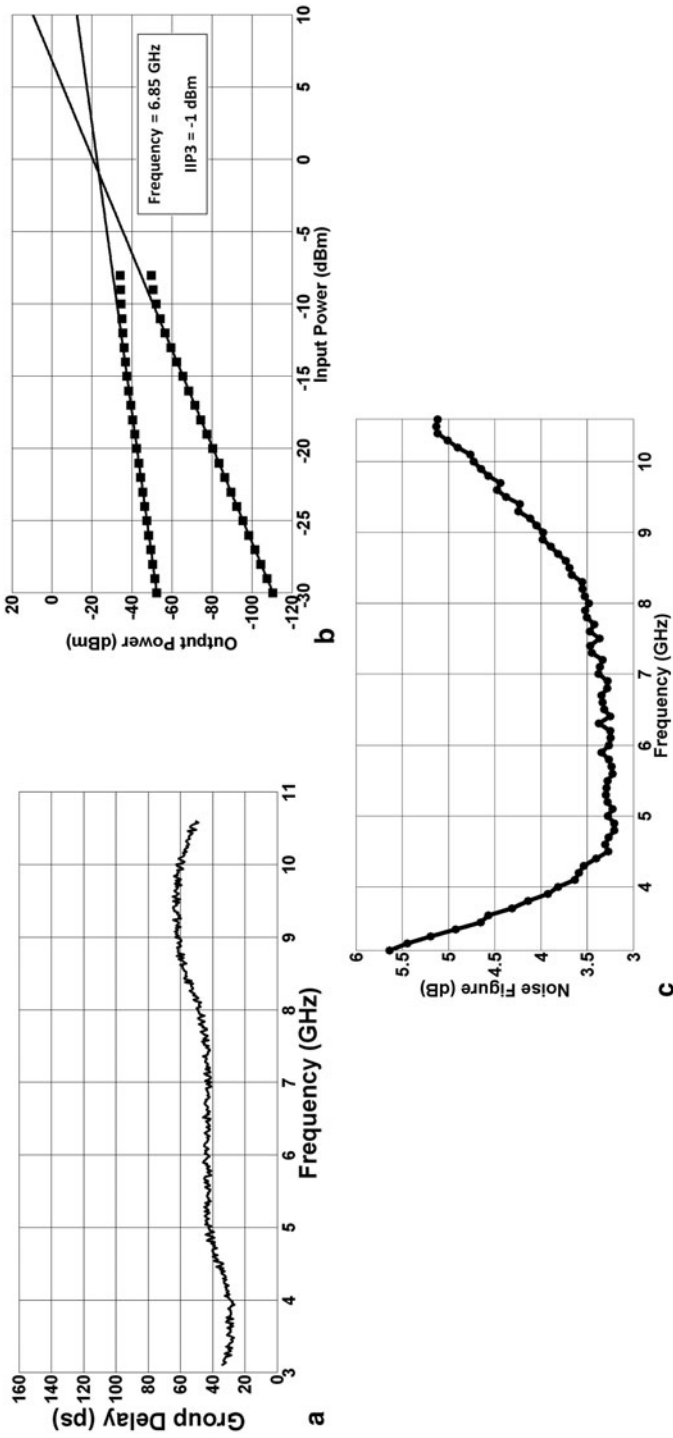


Fig. 18 Measured **a** linearity, **b** group delay, and **c** noise figure of designed low-noise amplifier (LNA)

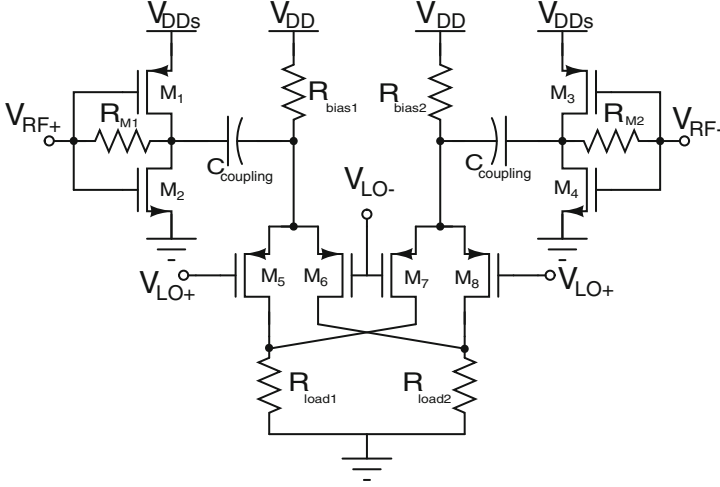


Fig. 19 Circuit schematic of the mixer core. V_{DDs} is the supply voltage of the subthreshold RF stage and is generated by internal biasing circuits

where I_{DC} is the RF stage bias current and $K_{RF} = \mu C_{ox} W/L$ is the process parameter of the RF-stage transistors. Above equations suggest an increase of RF stage biasing current as a way to improve performance of the mixer. However, it is clear that this current increase is confined to the power budget and cannot go above that. Also, despite the fact that increasing current will result in better linearity of the RF stage, for a stacked architecture, increasing the current will result in more voltage drop on load resistances and leaves less voltage swing for LO switches and consequently worse linearity. Considering noise in calculations makes the trade-off even more complicated. Noise of a Gilbert Cell is a combination of four different mechanisms: RF stage white noise, direct switching noise, indirect switching noise, and load thermal noise.

The total noise can be expressed as :

$$V_{o,n}^2 = 8kTR_L + 8kT\gamma \frac{R_L^2 I}{\pi A} + n \frac{8kT\gamma}{g_m} \left(\frac{2}{\pi} g_m R_L \right)^2, \quad (11)$$

where, the first term expresses the load noise, the second term is the switching noise, and the last term is due to the transconductance (i.e., RF) stage noise. As this equation suggests, reducing bias current of the switches as well as transconductance of the RF stage will result in a total noise reduction. This is in contradiction with the result of equations (8) and (9). It can be concluded that having independent DC currents for the RF and switching stages can relax the trade-off and result in a much more optimized biasing point.

Folded structure, with a decoupling capacitor that is suggested in this work will result in RF and LO stages that have completely independent DC biasing.

Here with the topology that is presented in Fig. 19, the RF stage is optimized to have the maximum conversion gain and linearity while the LO stage's bias is reduced

significantly to keep the power consumption and noise low, and have the minimum voltage drop on load resistances which causes better overall linearity. Also, in this work p-type MOSFETs are used for switches. Having PMOS switches in the LO stage, helps achieve the same overdrive voltage, and consequently similar linearity performance, with lower power consumption compared to the case using n-type metal-oxide semiconductor (NMOS) transistors [29]. In the design of the RF stage, an NMOS–PMOS stacked architecture is used. This will boost up the transconductance and consequently the conversion gain of the mixer. A high conversion gain (CG) for mixers relaxes the gain requirement of the LNA as its previous stage and will result in a better overall receiver design.

Furthermore, we took advantage of DC isolation of RF and LO stages, and designed the RF stage in the subthreshold region. With a good design, the same transconductance can be achieved with a significantly lower power consumption. Of course, this will result in a noise increase in the RF stage, but the switching noise is the dominant contributor in the total noise of the mixer. Our Cadence noise analysis results also show that M_5 – M_8 are the main contributors to the total noise with each of them being responsible for 13.4 % of the total noise. In RF stage, $R_{M1,2}$ are placed for input matching of the mixer and stabilize the gate and drain biasing voltage. Although mixer's input is connected to the LNA's output and it does not have to be matched to standard $50\ \Omega$, having these resistors as the parallel feedback for the RF stage will help us match the input resistance to desired value. R_{IN} can be written as

$$R_{IN} \approx \frac{R_M}{1 + (g_{m,n} + g_{m,p})(r_{ds,n} || r_{ds,p})}, \quad (12)$$

and using this equation, and knowing RF stage transistors' transconductance, R_M can be designed to make R_{IN} matched to the output of the previous stage.

Finally, R_{bias} is designed to set the DC voltage on the source of the switches and R_{load} is a passive load made of polysilicon to minimize the flicker noise at the output. In this design, the minimum length of 120 nm is chosen for M_{1-4} while the length of M_{5-8} is chosen to be 300 nm to reduce the flicker noise in the switches. Also, $W_{1-4} = 180\ \mu\text{m}$, $W_{5-8} = 200\ \mu\text{m}$, $R_{M1,2} = 2.8\ \text{k}\Omega$, $R_{bias1,2} = 600\ \Omega$, and $R_{load1,2} = 1.2\ \text{k}\Omega$. Finally, $V_{DDs} = 650\ \text{mV}$ is a reduced version of the supply voltage for the subthreshold RF stage, and is provided using internal biasing circuits.

One of the most common problems in UWB transceiver designs is that the LNA (as the first component after antenna) is usually single-ended and the output of this block should be connected to the mixer (multiplier) that has a differential input architecture. One solution to this is to use micro-strip lines and build a balun (balanced to unbalanced converter) to convert the single-ended signal to a differential one right after the antenna. With this solution, two single-ended LNAs can be used, and the output of each LNA can be connected to one input terminal of the mixer.

Although the phase precision of microwave baluns is good, and the differential signals are out-of-phase with a very good precision, having two LNAs that typically have a few inductors, doubles the required silicon area. Also, a passive balun implemented on-board is much bulkier than a circuit that is built on silicon. For these

Fig. 20 Circuit schematic of the wideband balun

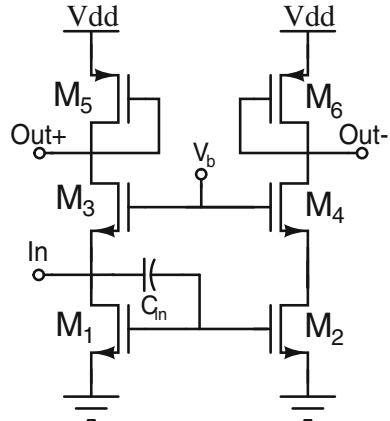
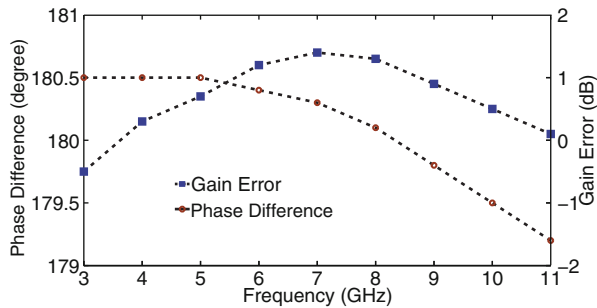


Fig. 21 Gain error and phase difference between the two outputs of the input balun



reasons we have developed a wideband balun, shown in Fig. 20, that converts the single ended input to differential with a high phase precision for the entire band of 3.1–10.6 GHz. In the balun design, we have used a cascode architecture which is to decrease phase error at the differential outputs. In addition to S–D (single to differential) conversion, having a balun at the input of a mixer will result in a reduction of the number of input pads by three (one RF signal and two grounds).

Also, in addition to the balun that is connected to the input of the mixer, another balun is separately laid-out. This helped us to characterize the performance of the balun and to de-embed its effect from core mixer’s performance. Figure 21 shows the gain error of the balun as well as the phase difference between the outputs.

As shown, the phase difference between the two outputs is very close to 180° for all the frequencies in the UWB band and the gain error is always less than 1.5 dB. Finally, for the intermediate frequency (IF) outputs of the mixer, a PRODYN balun is used to convert the differential outputs to a single-ended signal that can be connected to lab measurement equipment. Also, at the baseband IF outputs, DC-coupled common source buffers have been used to match to the lab equipment. The buffers are not shown in Fig. 19 and their power consumption is not included in total power consumption of the mixer. Figure 22a shows the measured conversion gain of the mixer for different input RF frequencies as well as different output IF frequencies.

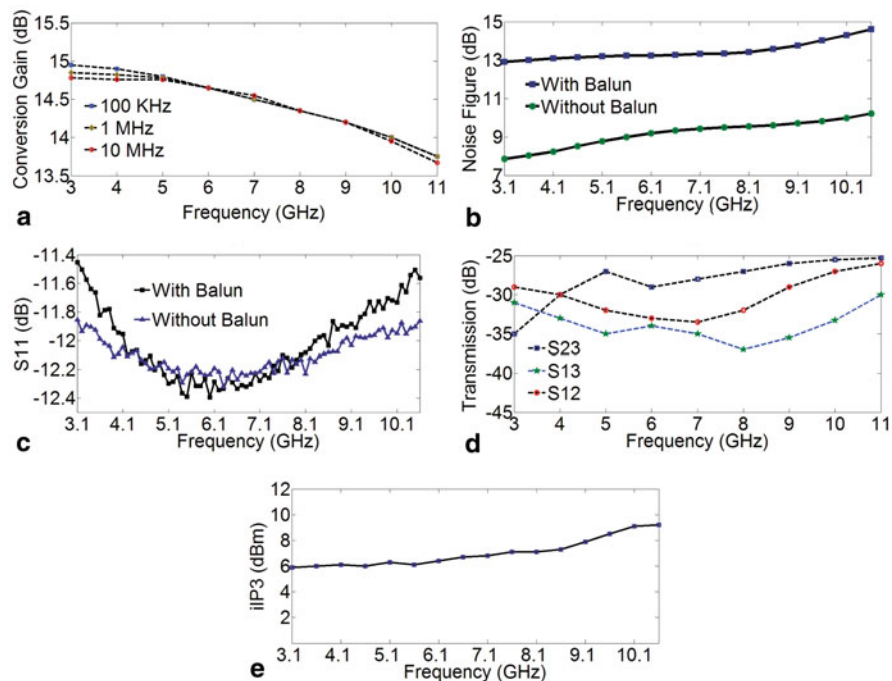


Fig. 22 Measured **a** conversion gain, **b** noise figure with and without the balun, **c** S_{11} , **d** port to port isolation, and **e** IIP3 of the designed mixer

As shown, the gain remains almost constant for various IF frequencies. Also, CG drops less than 3 dB, when the RF frequency is changed from 3 to 11 GHz. Figure 22b shows the noise figure of the designed circuit for both cases of with and without the balun. As shown, the core mixer (without a balun) has a minimum value of 6.9 dB and an average of 9.15 dB over the 7.5 GHz bandwidth. Figure 22c shows the input reflection coefficient for the RF port which shows excellent matching at this port for both cases of with and without the balun. Also, Fig. 22d shows the good performance of this design in terms of the port to port isolation. Finally, Fig. 22e provides IIP3 of the mixer for the whole range of RF frequencies.

References

1. A. Jemal, R. Siegel, E. Ward et al., Cancer statistics. *CA. Cancer. J. Clin.* **58**(2), 71–96 (2008)
2. E.M. Staderini, UWB radars in medicine. *IEEE. Aerosp. Electron. Syst. Mag.* **17**(1), 13–18 (2002)
3. E.C. Fear, X. Li, S.C. Hagness, M.A. Stuchly, Confocal microwave imaging for breast cancer detection: localization of tumors in three dimensions. *IEEE. Trans. Biomed. Eng.* **49**, 48–56 (2002)
4. W.T. Joines, Y. Zhang, C. Li, R.L. Jirtle, The measured electrical properties of normal and malignant human tissues from 50 to 900 MHz. *Med. Phys.* **21**, 547–550 (1994)

5. Y. Xie, B. Guo, L. Xu, J. Li, P. Stoica, Multistatic adaptive microwave imaging for early breast cancer detection. *IEEE Trans. Biomed. Eng.* **53**, 1647–1657 (2006)
6. L. Xu, S. Davis, S.C. Hagness, D. Weide, B. Veen, Microwave imaging via space–time beamforming: experimental investigation of tumor detection in multilayer breast phantoms. *IEEE Trans. Microwave & Theory Tech.* **52**, 1856–1865 (2004)
7. X. Xiao, T. Kikkawa, Study on the breast cancer detection by UWB microwave imaging. *IEEE*. 2008.
8. M. Patlak, S. Nass, I. Henderson, J. Lashof (eds.), *Mammography and beyond: developing technologies for the early detection of breast cancer*. (The National Academy Press, Washington, DC, 2001)
9. E.J. Bond, X. Li, S.C. Hagness, B.D. Van Veen, Microwave imaging via spacetime beamforming for early detection of breast cancer. *IEEE Trans. Antennas Propag.* **51**(8), 690–705 (2003).
10. J.G. Elmore, M.B. Barton, V.M. Mocerri, et al., Ten-year risk of false positive screening mammograms and clinical breast examinations. *N. Engl. J. Med.* **338**, 1089–1096 (1998)
11. K.R. Foster, H.P. Schwan, Dielectric properties of tissues and biological materials: a critical review. *Crit. Rev. Biomed. Eng.* **17**, 25–104 (1989)
12. K.S. Osterman, T.E. Kerner, D.B. Williams, A. Hartov, S. P. Poplack, K. D. Paulsen, Multifrequency electrical impedance imaging: preliminary in vivo experience in breast. *Physiol Meas.* **21**, 99–109 (1989)
13. J.L. Mueller, S. Siltanen, D. Isaacson, A direct reconstruction algorithm for electrical impedance tomography. *IEEE. Trans. Med. Imaging.* **216**, 555–559 (1989)
14. T.O. McBride, B.W. Pogue, S.D. Jiang, U.L. Osterberg, K.D. Paulsen, S.P. Poplack, Initial studies of in vivo absorbing and scattering heterogeneity in near-infrared tomographic breast imaging. *Opt. Lett.* **26**, 822–824 (2001)
15. John McCorkle, Ultra-wide bandwidth (UWB): gigabit wireless communications for battery operated consumer applications. 2005 Symposium on VLSI Circuits Digest of Technical Papers
16. K. Siwiak, Ultra-wide band radio: Introducing a new technology. *Proc. IEEE Veh. Technol. Conf.* **2**, 1088–1093 (May 2001)
17. Ultra-Wideband First Report and Order. Federal Communication Commission, Tech. Rep., February 2002
18. J.G. Proakis, *Digital Communications*. (McGraw-Hill, New York, 1995)
19. J. Lang, UWB chip design with embedded functionality, UWB Summit, Paris, France, CD Proceedings, (1989)
20. I. Oppermann, M. Hamalainen, J. Iinatti, *UWB Theory and Applications, Chapter 6* (Wiley, Chichester, 2004)
21. P.P. Mercier, D.C. Daly, A.P. Chandrakasan, An energy efficient all-digital UWB transmitter employing dual capacitively-coupled pulse-shaping drivers. *IEEE. J. Solid-State Circuits*, **44**(6), 1679–1688 (2009)
22. Y. Park, D. Wentzloff, An all-digital 12 pj/pulse ir-uwband transmitter synthesized from a standard cell library. *IEEE J. Solid-State Circuits*, **46**(5), 1147–1157 (2011)
23. P.P. Mercier, M. Bhardwaj, D.C. Daly, A.P. Chandrakasan, A low-voltage energy-sampling IR-UWB digital baseband employing quadratic correlation. *IEEE. J. Solid-State Circuits*. **45**(6), 1209–1219 (2010)
24. A. Bevilacqua, A.M. Niknejad, An ultrawideband CMOS low noise amplifier for 3.1–10.6 GHz wireless receivers. *IEEE. J. Solid-State Circuits*. **39**(12), 2259–2268 (Dec 2004)
25. S.-G. Lee, J.-K. Choi, Current-reuse bleeding mixer. *Electron. Lett.* **36**(8), 696–697 (Apr 2000)
26. S. Douss, F. Touati, M. Loulou, An RF-LO current-bleeding doubly balanced mixer for IEEE 802.15.3a UWBMB-OFDM standard receivers. *Int. J. Electron. Commun.* **62**, 490–495 (Jul 2008)
27. F. Mahmoudi, C. Salama, 8 GHz, 1 V, high linearity, low power CMOS active mixer. *Proc. IEEE Radio FrEq. Integr. Circuits Symp. Dig.* 401–404 (Jun 2004)
28. N. Poobuapheun, W.-H. Chen, Z. Boos, A. Niknejad, A 1.5-V 0.7–2.5-GHz CMOS quadrature demodulator for multiband direct-conversion receivers, *IEEE. J. Solid-State Circuits*. **42**(8), 1669–1677 (Aug 2007)
29. Y. Ding, R. Harjani, *High-Linearity CMOS RF Front-End Circuits*. (Springer, New York, 2005)